Title

Synthesis, Crystal Chemistry, and Electrochemical Properties of Li7–2x La3Zr2–x Mo x O12 (x = 0.1–0.4): Stabilization of the Cubic Garnet Polymorph via Substitution of Zr4+ by Mo6+

Journal

Inorganic Chemistry, 54(21)

ISSN

0020-1669

Authors

Rettenwander, Daniel
Welzl, Andreas
Cheng, Lei
et al.

Publication Date

2015-11-02

DOI

10.1021/acs.inorgchem.5b01895

Peer reviewed

Synthesis, Crystal Chemistry, and Electrochemical Properties of $Li_{7-2x}La_3Zr_{2-x}Mo_xO_{12}$ (x = 0.1 - 0.4): Stabilization of the Cubic Garnet Polymorph via Substitution of Zr^{4+} by Mo^{6+}

Daniel Rettenwander,[§*] Andreas Welzl,[#] Lei Cheng,[†,‡] Jürgen Fleig, [#] Maurizio Musso,[§] Emmanuelle Suard,[¶] Marca M. Doeff,[†] Günther. J. Redhammer,[§] and Georg Amthauer[§]

[§] Department of Materials Research and Physics, University of Salzburg, 5020 Salzburg, Austria.

[#] Institute for Chemical Technologies and Analytics, Vienna University of Technology, 1060 Vienna, Austria.

[†] Lawrence Berkeley National Laboratory, Environmental Energy Technologies Division, University of California, Berkeley, California, 94720, United States..

[‡] Department of Materials Science and Engineering, University of California, Berkeley, 94720, United States

[¶] Institute Laue-Langevin (ILL), Diffraction group, 71 avenue des Martyrs, 38000 Grenoble, France.

KEYWORDS LLZO, Li-ion conductor, garnet, molybdenum, solid electrolyte

ABSTRACT: Cubic $Li_7La_3Zr_2O_{12}$ (LLZO) garnets are exceptionally well suited to be used as solid electrolytes or protecting layers in “Beyond Li-ion Battery” concepts. Unfortunately, cubic LLZO is not stable at room temperature (RT) and has to be stabilized by supervalent dopants. In this study we demonstrate a new possibility to stabilize the cubic phase at RT via substitution of Zr^{4+} by Mo^{6+}. A Mo^{6+} content of 0.25 per formula unit (pfu) stabilizes the cubic LLZO phase and the solubility limit is about 0.3 Mo^{6+} pfu. Based on the results of neutron powder diffraction and Raman spectroscopy, Mo^{6+} is located at the octahedrally coordinated 16*a* site of the cubic garnet structure (space group *Ia*-3*d*). Since Mo^{6+} has a smaller ionic radius compared to Zr^{4+} the lattice parameter a_0 decreases almost linearly as a function of the Mo^{6+} content. The highest bulk Li-ion conductivity is found for the 0.25 pfu composition, with a typical room temperature value of 3.4×10^{-4} S cm^{-1}. An additional significant resistive contribution originating from the sample interior (most probably from grain boundaries) could be identified in impedance spectra. The latter strongly depends on the prehistory and increases significantly after annealing at 700 °C in ambient air. Cyclic voltammetry experiments on cells containing Mo^{6+} substituted LLZO indicates that the material is stable up to 6 V.

1. Introduction

$Li_7La_3Zr_2O_{12}$ garnet (LLZO) and its variants are exceptionally well suited for use as electrolytes in "Beyond Li-ion Battery" concepts that employ Li-metal anodes and high voltage cathode materials to enable cells with high energy and power densities. LLZO crystallizes either with tetragonal ($I4_1/acd$) or cubic ($Ia\text{-}3d$) symmetry (see Figure 1).[1,2] From the thermodynamic point of view, tetragonal LLZO, which shows a total Li-ion conductivity (reciprocal of the sum of the bulk and grain boundary resistance - for resistive grain boundaries only) that is approximately two orders of magnitude lower (< 10^{-6} S cm^{-1}) than that of the cubic modification (10^{-4} to 10^{-3} S cm^{-1}), is the more stable polymorph at room temperature (RT).[3] Fortunately, the cubic phase can be stabilized at RT by supervalent partial substitution of Li^+, La^{3+}, or Zr^{4+}. However, the substituents that induce this phase transition may strongly influence the Li-ion diffusivity and therefore the Li-ion conductivity. Much effort has been undertaken to understand these effects. Allen et al. investigated $Li_{6.75}La_3Zr_{1.75}Ta_{0.25}O_{12}$ (LLZTO) garnets substituted with Al or Ga and compared them to the parent compound. LLZTO had Li-ion conductivity that was twice as high (8.7×10^{-4} S cm^{-1}) as garnets substituted with Al^{3+} (3.7×10^{-4} S cm^{-1}) or Ga^{3+} (4.1×10^{-4} S cm^{-1}). They argued that the substituents located at the 24*d* and/or 96*h* sites of the Li-ion sub-lattice possibly had a blocking effect on diffusion in the garnet structure.[4] Recently several of us evaluated this assumption by studying the Li-ion diffusivity of $Li_{7-3x}Ga_{x-y}Al_yLa_3Zr_2O_{12}$ samples as a function of the site occupancy behavior of Al^{3+} and Ga^{3+}.[5]

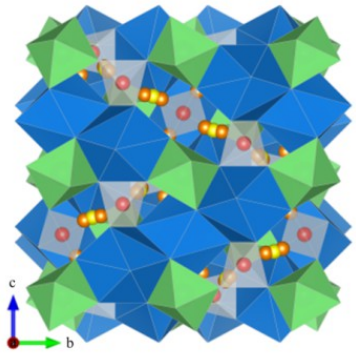

Figure 1. Crystal structure of cubic LLZO ($Ia\text{-}3d$). Blue dodecahedra (24*c*) are occupied by La^{3+}, green octahedra (16*a*) by Zr^{4+}. Li^+ are distributed over three sites *viz.* tetrahedrally coordinated (24*d*) sites represented by red spheres, octahedrally coordinated (48*g*) sites represented by yellow spheres, and distorted 4-fold coordinated (96*h*) sites represented by orange spheres.

It was shown that Ga^{3+} as well as Al^{3+} occupies both the 24*d* and 96*h* sites, but the blocking effect on Li-ion conductivity seemed to be much weaker than the influence of the unit-cell parameter a_0. Nevertheless, there is some interference with Li-ion diffusivity when the Li^+ sites are occupied with multivalent ions, as shown recently.[6] Therefore, effort is now being redirected towards finding suitable supervalent ions replacing La^{3+} or Zr^{4+} instead of Li^+. Here, we present the possibility of stabilizing the cubic LLZO polymorph through the partial substitution of Zr^{4+} by Mo^{6+}. $Li_{7-2x}La_3Zr_{2-x}Mo^{6+}{}_xO_{12}$ garnets (abbreviated $Zr_{2-x}Mo_x$) with x = 0.10 - 0.40 were synthesized by using solid state sintering methods. The samples were carefully characterized in terms of crystal chemistry, morphology, and electrochemical properties (*e.g.*, Li-ion conductivity, interfacial resistivity versus Li-metal electrodes, and the voltage stability window) by means of X-ray powder diffraction (XRPD), neutron powder diffraction (NPD), scanning electron spectroscopy (SEM), Raman spectroscopy, electrochemical impedance spectroscopy (EIS) and cyclic voltammetry (CV).

2. Experimental

Synthesis of $Li_{7-2x}La_3Zr_{2-x}Mo^{6+}{}_xO_{12}$ garnets with x = 0.10-0.40 were performed by high-temperature sintering. The starting materials were Li_2CO_3 (99 %, Merck), La_2O_3 (99.99 %, Aldrich), ZrO_2 (99.0 %, Aldrich) and MoO_3 (99.98 %, Aldrich). Li_2CO_3 was mixed with the various oxides in the desired proportions, and intimately ground together using a hand mortar, a pestle, and isopropanol. These mixtures were uniaxially pressed to a pellet, calcined at 850 °C for 4 h with a heating rate of 5 °C/min and then cooled in the furnace to approximately 200 °C. Samples mixed with isopropanol were milled in a Fritch Pulverisette 7 ball mill for 2 h (12 times 550 rpm for 5 min + 5 min break). Finally, powders were isostatically pressed (24 kbar) to form pellets and sintered at 1230 °C for 4 h, with a heating rate of 20.5 °C/min, and afterwards cooled to RT.

XRPD measurements were performed using a Bruker D8 Advance DaVinci Design diffractometer (Lynxeye solid state detector) with CuK_α radiation. This was done in order to characterize the synthetic products and to identify all phases present, including determination of the symmetry and unit-cell dimension of the garnets. Data was collected between 10° and 140° 2θ. The lattice parameter a_0 was determined by using an internal standard (Si with a = 5.43088 Å) and performing Rietveld refinement with the program Topas V4.2 (Bruker AXS).

NPD The neutron diffraction experiment was done at the Institut Laue-Langevin, ILL, in Grenoble (France). Powder diffraction data were acquired in constant wavelength mode (λ = 1.594 Å) using the D2B diffractometer on an 8.5 g batch contained in a 14 mm diameter vanadium sample can at 25 °C. Experiments were performed in the range 5.8 ° ≤ 2θ ≤ 159.7 °, step width 0.04 °. Data

treatment and refinement was done using the FULLPROF-suite of programs[6] with the pseudo-Voigt peak shape function. Due to the significant absorption of neutron radiation by Li an absorption correction was applied. The atomic displacement parameters were modelled in the isotropic form, except for the oxygen atom; any refinement with anisotropic displacement parameters of the other sites led to non-positive definite atomic displacement parameters and high correlations with the occupation numbers, thus unphysical data.

SEM analysis was made using a ZEISS Ultra Plus device. Small polycrystalline chips, taken from the larger pellets, were embedded in an epoxy holder and the surface was ground and then polished using diamond paste. For the analysis, special attention was made with regard to extra phases, grain sizes, grain boundaries and textures using a back-scattered electron detector (BSE). Energy dispersive spectroscopy (EDS) measurements were undertaken to measure the atomic ratios of La, Zr, and Mo to determine qualitatively the upper incorporation of Mo in LLZO.

RAMAN spectra were recorded at room temperature in the spectral range of 50−3500 cm^{-1} using a Thermo DXR Raman microscope with a 10 mW internal laser light source with excitation wavelength at 780 nm.

EIS measurements were carried out to investigate the Li-ion conductivity. Pt thin films were used as electrodes and were sputter deposited with a thickness of 200 nm on top of ca. 10 nm Ti, which improved the adhesion between the sample and the electrode. For the EIS measurements, a Novocontrol Alpha analyzer was used in the frequency range of 3×10^6—10^1 Hz. A Julabo F-25 HE circulator was employed for cooling and heating the samples under investigation. Set temperatures between -12 °C and 25 °C (with some measurements at 40 °C) were used, leading to true sample temperatures from ca. -8 °C to 36 °C. In the following, true sample temperatures, measured by a thermocouple, are indicated in all diagrams. An additional impedance spectrum was taken for a Li/Garnet/Li sample at room temperature in an Ar glovebox. For this, metallic lithium was first applied on the surfaces of pellet and the pellet was sandwiched with two lithium foil disks in a Swagelok type cell (see Ref 18).

CV measurements were performed using a Li/Garnet/Au configuration to assess the electrochemical window of garnet pellets. The Au blocking electrode was sputtered on one surface of the garnet pellet and the reversible Li electrode was applied on the other side of the pellet. Ni foam was used as current collectors. The measurement was carried out inside an Ar glovebox. The cell was scanned at a rate of 2 mV/min in the potential range from -0.5 V to 6 V vs. Li/Li^+.

3. Results & Discussion

3.1 Phase composition of the solid solutions studied by XRPD

The dense pellets obtained after the final sintering step were slightly yellowish in color, and after grinding the powder became white. The XRPD patterns of $Zr_{2-x}Mo_x$ garnets with x = 0.10—0.40 are shown in Figure 2 together with reference XRPD patterns for cubic and tetragonal structures.[1,2]

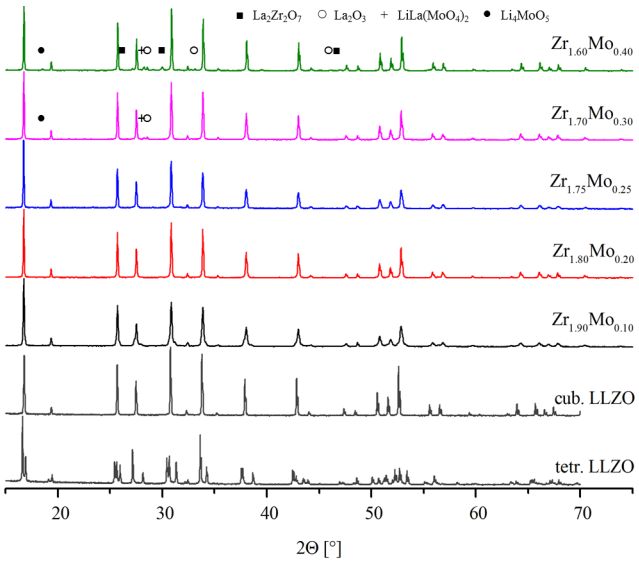

Figure 2. XRPD pattern of $Li_{7-2x}La_3Zr_{2-x}Mo_xO_{12}$, with x = 0.10—0.40. The tetragonal and the cubic diffraction pattern of LLZO are shown for comparison.

Sample $Zr_{1.90}Mo_{0.10}$ exhibits reflections indicating that both cubic (~75 %) and tetragonal (~25 %) garnets are present. By increasing the amount of Mo^{6+} to 0.20 pfu the amount of the cubic phase increased (~83 %) whereas the tetragonal phase decreased (~17 %). With a Mo^{6+} content of 0.25 pfu no phases other than cubic LLZO were found in the synthetic product. When the Mo^{6+} content was 0.3 pfu and above, a mixture of extra phases ($Zr_{1.70}Mo_{0.30}$: $La_2Zr_2O_7$, La_2O_3, $LiLa(MoO_4)_2$, Li_4MoO_5; $Zr_{1.60}Mo_{0.40}$: $La_2Zr_2O_7$, La_2O_3, $LiLa(MoO_4)_2$, Li_4MoO_5) appeared in addition to the cubic LLZO in the product and increased as the Mo^{6+} content rose.

3.2 Morphology and phases as studied by SEM methods

BSE photos of polycrystalline chips of the samples are shown in Figure 3.

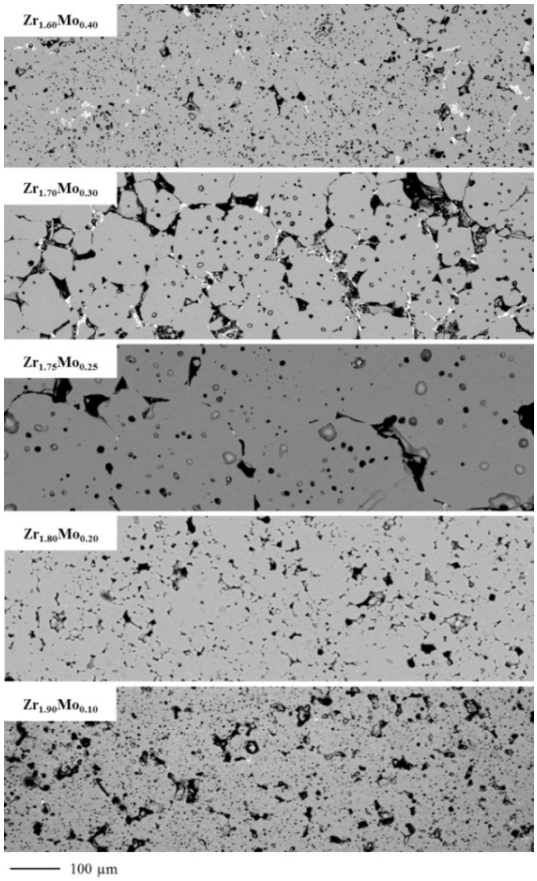

Figure 3. BSE images of the polished embedded pellets of $Li_{7-2x}La_3Zr_{2-x}Mo_xO_{12}$, with x = 0.1—0.4.

The sample $Zr_{1.90}Mo_{0.10}$ has large porous and poorly connected grains with diameters of about 100 µm. With a Mo^{6+} content of 0.2 pfu, the grain size decreased to about 50 µm. Compared to $Zr_{1.90}Mo_{0.10}$, the sample seemed to be denser, and grains were better connected to each other. Sample $Zr_{1.75}Mo_{0.25}$ showed a significant increase of the grain sizes (in the range of 200 µm), which may be related to the overall stabilization of the cubic phase. The samples showed less porosity, but there were still large voids between grains. With a Mo^{6+} content of ≥ 0.3 pfu, smaller grains (50-100 µm) were found and extra phases occurred (see Figures 2 and 3). The density decreased and the porosity within the grains increased with higher Mo^{6+} and impurity content. The qualitative chemical analyses on the polished cross-sections of several grains using EDS are consistent with the substitution of Zr^{4+} by Mo^{6+} and an upper incorporation limit close to 0.3 Mo pfu (*e.g.*, $Zr_{1.70}Mo_{0.30}$ □ $La_{3.00}Zr_{1.70}Mo_{0.28}$ and $Zr_{1.60}Mo_{0.40}$ □ $La_{2.94}Zr_{1.77}Mo_{0.30}$).

3.3 Unit-cell parameter of LLZO as a function of the Mo^{6+} content as studied by diffraction methods

The unit-cell parameters of the cubic LLZO phases, a_0, as a function of the amount of Mo^{6+} in LLZO are shown in Figure 4.

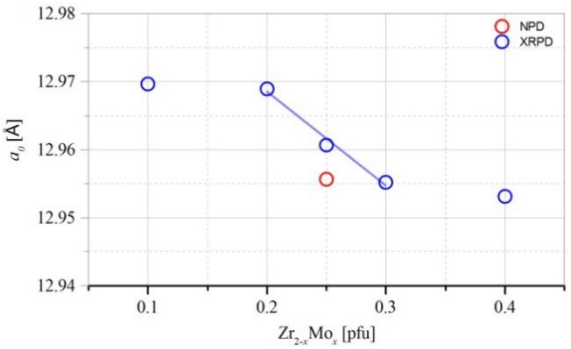

Figure 4. Lattice parameter of the cubic LLZO phase, a_o, versus the nominal Mo content (x = 0.1—0.4) in $Li_{7-2x}La_3Zr_{2-x}Mo_xO_{12}$.

There is a decrease in a_0 with increasing Mo^{6+} content with an almost linear relationship between x = 0.20 to 0.30. The decrease of a_0 can be related to *(i)* the smaller ionic radius of Mo^{6+} (r^{VI} = 0.60 Å) compared to Zr^{4+} (r^{VI} = 0.72 Å)[8] and/or *(ii)* the reduction of the Li^+ content, (Mo^{6+} ↔ Zr^{4+} + 2 Li^+). The unit-cell parameters are on the average around 12.964 Å, which has recently been proposed to be the optimum for high ionic conductivities.[9] Because the unit-cell parameter remained unchanged at a Mo^{6+} content of 0.4 pfu, we assume an upper incorporation limit of about 0.3 Mo^{6+} pfu, which is in agreement with the EDS results (see 3.2 above).

3.4 Site occupation behavior in LLZO – long range properties as studied by NPD

As shown by XRPD and SEM, (see 3.2 and 3.3 above) the $Zr_{1.75}Mo_{0.25}$ is the only composition that is composed of the cubic polymorph only and was therefore used for the NPD study. The Rietveld refinement results of the NPD pattern shown in Figure 5 and given in Table 1 give strong evidence that Mo^{6+} mainly substitutes Zr^{4+} at the octahedral 16*a* site, yielding 0.256(21) Mo^{6+} pfu, a value which perfectly matches the nominal stoichiometry; tests with Mo^{6+} on the La^{3+} site gave negative occupation numbers, excluding this site for substitution. In a first model of cationic distribution, the tetrahedral 24*d* site is exclusively occupied by Li^+, thereby giving an approximately half filled occupation, the remaining being empty, while the interstitial octahedral coordinated 96*h* position hosts about 4.34(2) Li^+ pfu. It might be noted, however, that with this model, the Rietveld refinements yield a formula, which is not balanced in charge, but has a deficit of about 0.63 positive charges, probably as Li^+ content. Allowing anisotropic refinement of all atoms, by using non-positive definite displacement parameters, did not significantly change the occupation numbers on 16*a* and 24*d* sites, but increased that of the 96*h* site to 0.42(4), distinctly reducing the deficit in positive charge. It is assumed that the isotropic handling of atoms fails to describe the strong anisotropy,

especially of the Li2 site, thus giving Li^+ contents on Li2 that are too low.

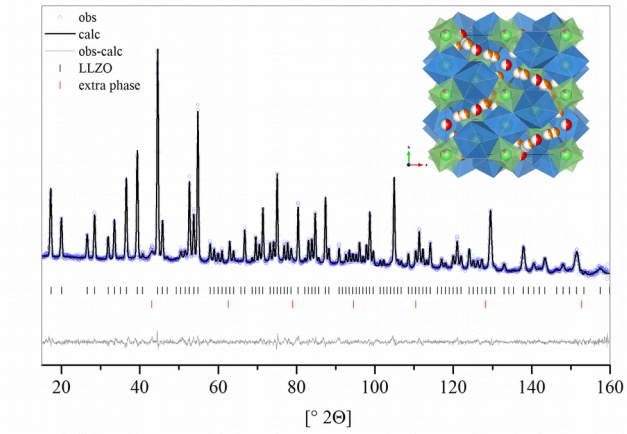

Figure 5. The observed (obs), calculated (calc), and difference patterns (obs-calc) for the Rietveld refinement from neutron diffraction of nominal $Li_{6.50}La_3Zr_{1.75x}Mo_{0.25}O_{12}$.The short vertical lines below the profiles mark the peak positions of all possible Bragg reflections of cubic LLZO (black) and a unknown Li-containing extra phase, which remain undetected by other analytical methods (red); (Inset) Crystal structure of cubic LLZO (*Ia*-3*d*) based on the results of Rietveld refinement given in Table 1.

Table 1. Neutron powder diffraction data of $Li_{7-2x}La_3Zr_{2-x}Mo^{6+}{}_xO_{12}$ determined through Rietveld Refinement.

	Site	*x/a, y/b, z/c*	U_{iso}[a]	Occ.[c]
Li1	24 *d*	0, 3/4, 5/8	3.0(5) [b]	.50(2)
Li2	96 *h*	.0996(1), .6829(1), .5834(1)	4.2(5)	.362(1)
La	24 *c*	0, 1/4, 1/8	1.54(5)	1.0000
Zr	16 *a*	0, 0, 0	1.71(5)	.87138
Mo	16 *a*	0, 0, 0	1.71(5)	.12864
O	96 *h*	-.03125(1), .05443(1), .1489(1)	2.18(9)	1.0000

Space group: *Ia*-3*d* (No. 230) and $Z = 8$
Lattice parameter: $a = b = c = 12.9556(2)$
R-factors: $R = 2.6685$, $chi^2 = 1.9451$, $R_I = 4.1824$
[a] ×100 [Å²]; [b] Constraint on isotropic atomic displacement: $U_{iso}(Zr) = U_{iso}(Mo)$; [c] Occupation factor

A second model of cationic substitution assumes small amounts of Mo^{6+} also on the tetrahedral 24*d* sites. As Li^+ has a negative scattering length (Mo has a positive one) it is also possible to put Mo^{6+} on the tetrahedral site and obtain comparably good refinements. However this gives an unrealistically high Mo^{6+} of 0.7 pfu and Li-contents that are too low, when a full occupation of the tetrahedral site is assumed. It is possible to find a reasonable, charge balanced cationic distribution, by manipulating the Mo^{6+} content at 24*d* by hand, which gives a plausible cationic distribution. This is the case when 0.048 formula units Mo^{6+} are placed on the tetrahedral sites, giving a refined Li content of 1.68 pfu at 24*d* and 4.37(2) Li^+ on 96*h*, *i.e.*, almost identical values. However, the cationic distribution at the 16*a* site–also slightly changes, giving 0.304(23) Mo^{6+} pfu. The total of 0.35 Mo^{6+} pfu is distinctly higher than the nominal stoichiometry. All in all we prefer refinement model 1 (see Table 1), as it gives the more realistic Mo^{6+} content. The models are different in site occupancies only, atomic coordinates and isotropic/anisotropic displacement parameters do not change.

3.5 Site occupation behavior in LLZO – short range properties as studied by Raman spectroscopy

Additional evidence for the above chosen model 1 can be obtained by Raman spectroscopy. The Raman spectra shown in Figure 6 were collected for each sample to determine cubic and tetragonal phase contributions in each product as well as the site preference of Mo^{6+} in the garnet oxygen framework.

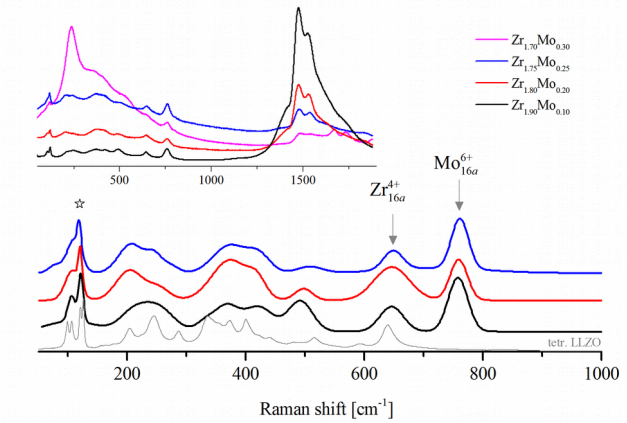

Figure 6. Baseline corrected Raman spectra, obtained with laser excitation at 780 nm, of $Li_{7-2x}La_3Zr_{2-x}Mo_xO_{12}$, with $x = 0.1$—0.3 and tetragonal LLZO for comparison. The uncorrected spectra are shown in the inset. The spectra are normalized to the Raman band marked by a star. The bands at about 110 cm^{-1} are used to distinguish between the cubic and the tetragonal polymorph. In the range between 600 and 800 cm-1 two t_{2g} bands are observable which correspond most probably to Zr^{4+} and Mo^{6+} in LLZO occupying the 6-fold coordinated 16*a* site in space group *Ia*-3*d*.

Because of overlapping features in the Raman spectra of probably undetected small amounts of luminescing extra phases, the spectra were baseline corrected and analyzed for qualitative

analysis only. A Raman study of LLZO has been reported by Tietz et al.[10] The partial substitution of Zr^{4+} with Ta^{5+} was investigated later on by Thompson et al.[10] They proposed that the band near 650 cm^{-1} was related to the stretching of the ZrO_6 octahedra. When Ta^{5+} was added to the system, an additional band near 750 cm^{-1} appears and increases in intensity with higher amounts of Ta^{5+}.[10] Because bands near 750 cm^{-1} seem to correspond to stretching of an octahedron other than ZrO_6, the analog band in our spectra was assigned to a MoO_6 octahedron. This gives additional evidence for the site occupancy of Mo^{6+} at the octahedral 16*a* site in the oxygen garnet framework. Because Raman can be used to distinguish cubic and tetragonal LLZO phases the method can also be used to check phase composition. Tietz et al. showed that the bands near 110 cm^{-1} are most diagnostic of this.[10] The reduction of symmetry from cubic to tetragonal is shown by a splitting of the vibrational modes. In our samples, this feature is not well resolved because of the broad line shape. Nevertheless, it appears that the line shape of those modes at about 110 cm^{-1} converge with increasing Mo^{6+} content. This is similar to the observations made by Thompson et al. for $Li_7La_3Zr_{2-x}Ta_xO_{12}$ garnets with increasing amount of Ta^{5+} up to 0.25 Ta^{5+} pfu. Above this, they found a superposition of the cubic as well as tetragonal phase in the products. The Raman spectra of the product with a Mo^{6+} content of 0.25 in this study looks almost identical to the spectra reported for single phase cubic $Li_7La_3Zr_{1.5}Ta_{0.5}O_{12}$.[11] Both the substitution of Zr^{4+} by 0.5 Ta^{5+} or by 0.25 Mo^{6+} pfu leads to a decrease in the Li^+ content to about 6.5 pfu, which also seems to be necessary to stabilize the cubic garnet phase.

3.6.1 Investigating the Li-ion conduction in Mo^{6+} doped LLZO by means of impedance spectroscopy

Impedance spectra were measured for as prepared samples of all compositions at different temperatures. Figure 7 displays the relevant data, measured at RT = 23.5 °C (a) and lowest temperature (b), including magnifications of the high frequency parts. Common to all samples is the existence of a more or less complete high frequency semicircle at low temperatures. For some samples, this is followed by a depressed intermediate frequency arc. Again common to all samples is a strong increase of the imaginary part of the impedance towards low frequencies, with an almost constant angle in the complex impedance plane, partly resembling the onset of a large depressed arc. The low frequency impedance feature depends on the electrode material (see also below) and can be attributed to electrode effects. In a certain frequency range it can be described by a resistor in parallel to a constant phase element (CPE) with impedance

$$Z_{CPE} = 1/(i\omega)^n Q \quad . \qquad (1)$$

where ω is the angular frequency and Q and n are fit parameters. This electrode equivalent circuit helps with analysis of the sample-specific high frequency features but does not imply any mechanistic information. A discussion of the exact electrode reaction mechanisms causing this feature (diffusion or charge transfer processes, etc.) is beyond the scope of this paper.

The high frequency arc is attributed to the bulk Li-ion conduction (σ_{bulk}) of the LLZO samples; see also the discussion of capacitances below. For a proper fit analysis of the σ_{bulk} and permittivity (ε_1), another resistor (R_1) in parallel to a constant phase element (CPE_1) was used.

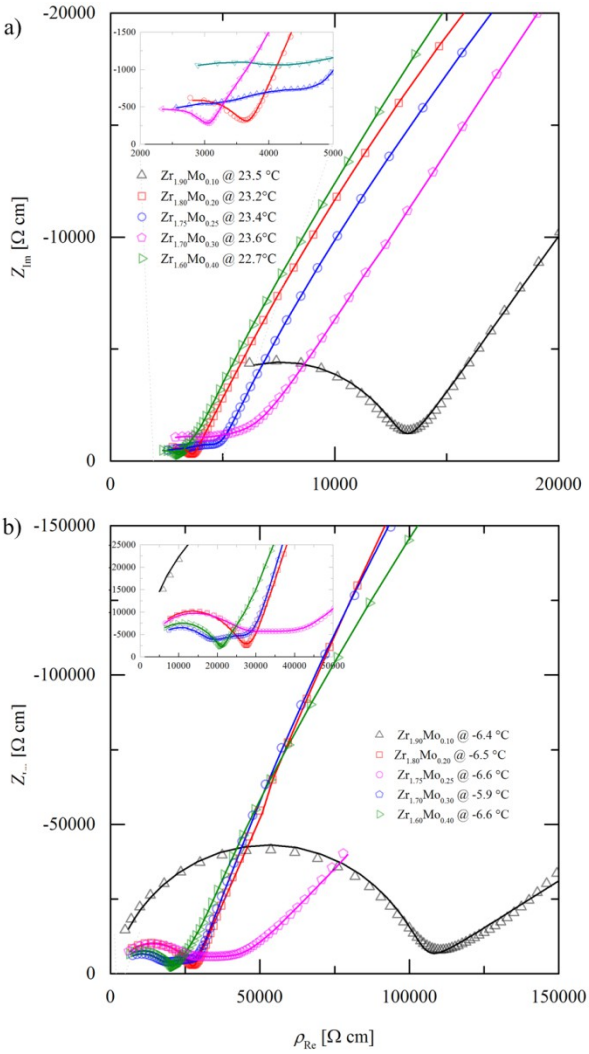

Figure 7. Impedance spectra of as prepared LLZO samples with different Mo doping concentration measured at room temperature (a) and at the lowest temperature (ca. -6 °C, a,b). For both temperatures, different magnifications are shown and solid fit lines (equivalent circuit model in Fig. 8) are included. Data reflects resistivity, ρ (normalized to the sample area and thickness).

Capacitances were then calculated from fit parameters Q_1 and n_1 according to Ref. [12]:

$$C_1 = \left(R_1^{1-n_1} Q_1 \right)^{1/n_1} \qquad (2)$$

Particularly for samples with low bulk resistances (R_1), the unavoidable inductance (L) due to wiring significantly affects the data and has to be added to the equivalent circuit. Finally, a proper description of the partial intermediate frequency feature is necessary to obtain a reliable fit of the spectra and thus of the σ_{bulk}. As required, *e.g.*, for $Zr_{1.75}Mo_{0.25}$, $Zr_{1.70}Mo_{0.30}$, and $Zr_{1.60}Mo_{0.40}$, this feature was again approximated by a resistor in parallel to a constant phase element. A mechanistic discussion of this second (*i.e.*, intermediate frequency) arc is given below. The resulting equivalent circuit is shown in Figure 8 and fits all measurement data acceptably well; fit examples are shown in Figure 7, 8 and 9.

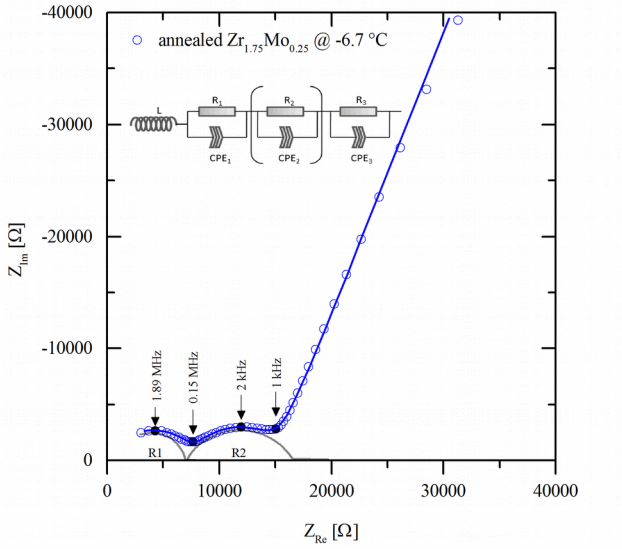

Figure 8. Equivalent circuit used to fit all spectra. Markers indicate frequencies of experimental data. In some cases R_2, CPE_2 was not required.

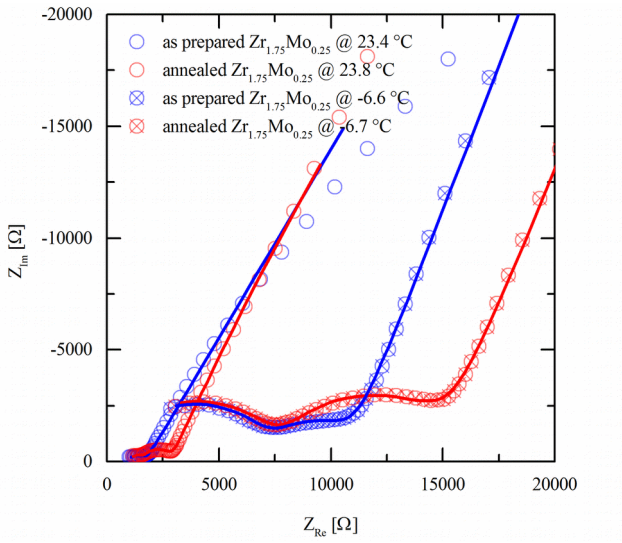

Figure 9. Impedance spectra of $Zr_{1.75}Mo_{0.25}$ before and after annealing at 700 °C, measured in the range of ca. -7 °C and RT. Clearly, the intermediate frequency arc became more pronounced when the sample was annealed. Solid lines are fits using the model in Figure 8. Markers indicate frequencies of experimental data.

3.6.2 Objections to the impedance data analysis

Two possible objections to such a data analysis are considered: First, one may question the appropriateness of a *R*-CPE element for describing partly almost horizontal line in the intermediate frequency range. Here, an additional phenomenon comes into play. After annealing the samples at 700 °C for a few minutes (without the deposited electrode) to remove Li_2CO_3 depositions and H incorporation formed by degradation/ageing processes, the high frequency bulk arc is only slightly changed, while the intermediate frequency feature becomes more pronounced and larger (Figure 9). Moreover, the second arc becomes measurable for all samples, irrespective of whether it was already visible before annealing (compare Figure 7 and Figure S1). For annealed samples, the circuit in Figure 8 describes the data very well, supporting the approach of applying this model to spectra obtained on as-prepared samples. However, particularly for $Zr_{1.70}Mo_{0.30}$ before annealing and $Zr_{1.90}Mo_{0.10}$ after annealing, the model is at its limits: *n* values of the constant phase element CPE_2 drop below 0.55 and thus also a proper quantification of the bulk arc becomes somewhat questionable. This is most probably the reason behind the significant scattering of conductivity data found for a few samples (see below).

Second, it is obvious that for some samples, the onset of a separate bulk arc is out of the measured frequency range at the highest temperatures. The influence of the bulk arc on the spectrum is still apparent, but it is hidden in the spur; the minimum of the imaginary part is presumed to appear at higher frequencies than can be measured in these experiments. This raises the question of whether reliable bulk conductivity can still be obtained.

To further investigate this, Figure 10 shows a series of impedance spectra measured for $Zr_{1.75}Mo_{0.25}$ between -9.5 °C and RT after annealing.

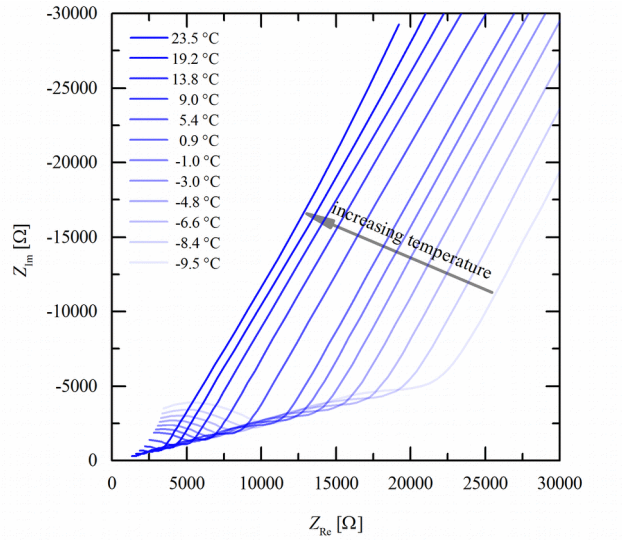

Figure 10. Temperature dependence of impedance spectra for an as-prepared $Zr_{1.75}Mo_{0.25}$. The high frequency arc diminishes in magnitude as the temperature was raised.

In this series, the spectra change from an obvious bulk arc at low temperatures to one in which the spur predominates at room temperature. However, when starting the fitting procedure at low temperatures and always using the fit results as starting values of the next fit procedure at the next higher temperature, very consistent capacitance and resistance data can be obtained (see below). Capacitances from CPE_1 did not vary too much and conductivities close to room temperature are in line with those extrapolated from the very reliable low temperature conductivity data. Additional evidence for the meaningfulness of this analysis comes from a measurement performed on $Zr_{1.75}Mo_{0.25}$ of a different batch series with reversible Li electrodes, see below. Hence, we consider this analysis as meaningful and able to deduce the proper bulk materials parameters.

3.6.3 The bulk transport of Li-ions in Mo-doped LLZO

A strong argument in favor of R_1 representing a bulk transport process is the existence of a meaningful geometrical bulk capacitance in parallel. C_1 values are in the 10 pF range and calculating a relative permittivity $\varepsilon_{r,1}$ from sample area A and sample thickness d (ε_0 = vacuum permittivity) according to

$$\varepsilon_{r,1} = C_1 d / A \varepsilon_0 \quad (3)$$

leads to values of the order of 40-60. The relative permittivities for all temperatures and samples before and after annealing are summarized in Figure S2. The increase close to room temperature, found for some samples, reflects the uncertainty due to absence of large parts of the high frequency arcs. The $\varepsilon_{r,1}$ values of ca. 40-60 are very realistic bulk values for oxides with significant ionic polarization (and similar to ε_r of ZrO_2[13]), and thus support the interpretation of R_1 as a bulk property. We cannot exclude the existence of highly conducting grain boundaries, since those would only add an additional resistor in parallel to R_1 and thus do not change the shape of the spectrum and the capacitance.[14,15] However, to date conclusive experimental evidence supporting the assumption of fast grain boundary conduction in LLZO is not available in the literature. Accordingly, the bulk conductivity, σ_{bulk}, of Li-ions in our LLZO samples was determined from R_1 by

$$\sigma_{bulk} = d / R_1 A \quad . \quad (4)$$

Arrhenius plots of the Li-ion conductivities are shown in Figure 11 for all samples before (a) and after annealing (b). Data scattering can be largely attributed to fitting inaccuracies caused by the intermediate frequency arc (see above). Before annealing (as-prepared), Li-ion conductivities of most compositions (except $Zr_{1.90}Mo_{0.10}$) coincide at RT. All Arrhenius fits lead to ca. 3.4×10^{-4} S cm^{-1}, exact values are given in Table 2.

Slight differences in activation energies E_a (see Table 2) cause some discrimination at low temperatures with $Zr_{1.75}Mo_{0.25}$ exhibiting the highest low temperature Li-ion conductivity. Annealing at 700 °C leaves the σ_{bulk} of $Zr_{1.80}Mo_{0.20}$ and $Zr_{1.75}Mo_{0.25}$ virtually identical, (~3.4×10^{-4} S cm^{-1}) at RT, with the best low temperature σ_{bulk} found for $Zr_{1.75}Mo_{0.25}$.

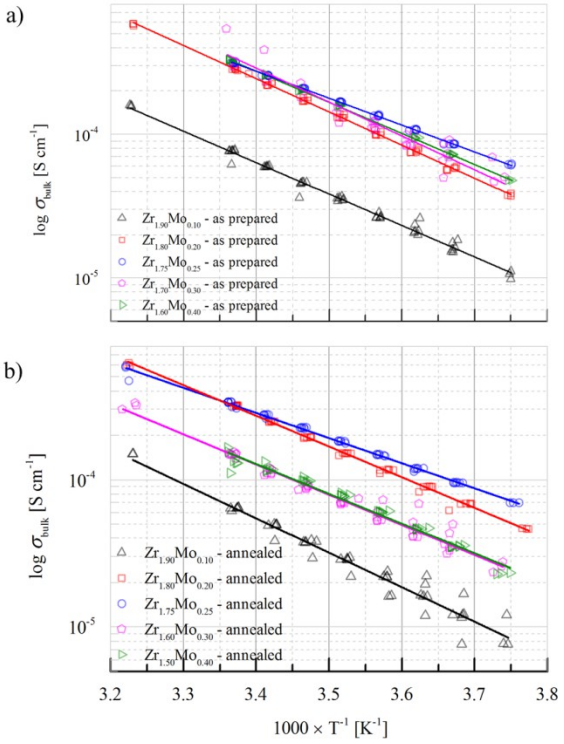

Figure 11: Temperature dependent bulk conductivities for as-prepared (a) and annealed (b) samples of different Mo doping content.

Table 2. Activation energies, $E_{a,1}$ (bulk) and $E_{a,2}$ (intermediated arc[a]) of σ_{bulk}·T, and bulk conductivities, σ_{bulk}, of $Zr_{2-x}Mo_x$, with x = 0.0 – 0.4 at RT according to the Arrhenius fit.[b]

x	$E_{a,1}{}^{a}_{p}$ [eV]	$E_{a,1}{}^{a}_{n}$ [eV]	$E_{a,2}{}^{a}_{p}$ [eV]	$E_{a,2}{}^{a}_{n}$ [eV]	$\sigma_{bulk}{}^{ap}$ [S cm^{-1}]	$\sigma_{bulk}{}^{an}$ [S cm^{-1}]
0.10	0.46	0.48	-	0.44	8.00 x 10^{-5}	6.82 x 10^{-5}
0.20	0.48	0.44	-	0.62	3.11 x 10^{-4}	3.38 x 10^{-4}
0.25	0.39	0.36	0.44	0.43	3.33 x 10^{-4}	3.40 x 10^{-4}
0.30	0.49	0.44	0.40	0.56	3.69 x 10^{-4}	1.00 x 10^{-4}
0.40	0.48	0.43	0.65	0.66	3.40 x 10^{-4}	1.58 x 10^{-4}

[a] Activation energies of the intermediate arc, see in the text below; [b] Samples as prepared are abbreviated ap and samples after annealing an

The samples $Zr_{1.70}Mo_{0.30}$ and $Zr_{1.60}Mo_{0.40}$ exhibit a drop in conductivity by ca. a factor of 2. This decrease of Li-ion conductivity may be related to phase changes since those samples are not phase-pure. The E_a values of σ_{bulk}·T are in the range of 0.36-0.49 eV (see Table 2) and the best Li-ion conducting composition ($Zr_{1.75}Mo_{0.25}$) exhibits the lowest value (0.39 eV as prepared and 0.36 eV after annealing, respectively). All other samples have very similar activation energies with an average of ca. 0.45 eV. Activation energies are thus compatible with other Li-oxide garnets.[17] See also Figure S3 and S4 for further discussion, particularly of σ_{bulk} variations of nominally identical samples from different batches.

3.6.4 The intermediate frequency arc – Grain boundary or not?

Intermediate frequency impedance features are often found in literature[16] and are sometimes interpreted in terms of resistive grain boundaries.[3,17] In other cases, an additional arc in the spectra is attributed to the electrode/LLZO interface.[18-20] For a more detailed analysis of the intermediate frequency arcs observed in the Nyquist plots of the samples in this study, analysis of the corresponding capacitance is helpful. This may give information on the location of the resistor R_2. Here, Eq. (3) cannot simply be applied to C_2 since the relevant thickness is unknown; in case of one-dimensional current flow we should use the thickness of the region(s) causing the resistance.

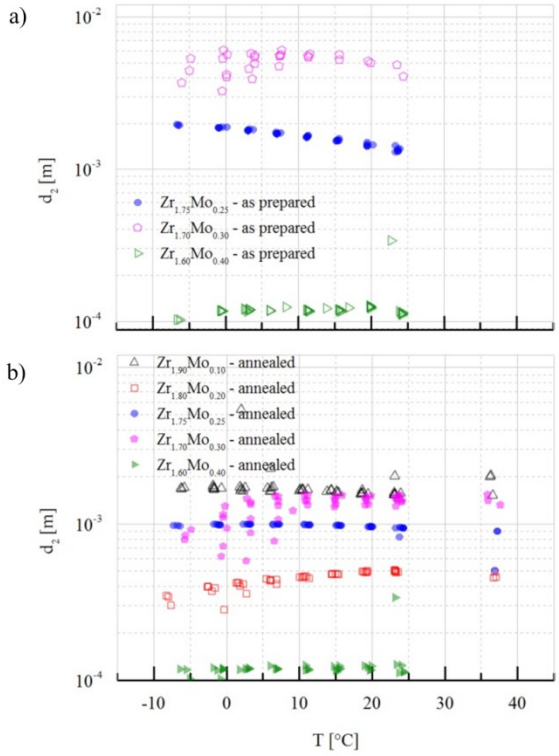

Figure 12. Thickness of the region causing the intermediate frequency arc, calculated from C_2 by assuming bulk permittivity. (a) Values of as-prepared samples for different temperatures. (b) Values of annealed samples for different temperatures. All open symbols refer to samples for which the exponent n of the CPE element is on average below 0.6. Since bulk capacitances and thus bulk permittivities become less accurate for increasing temperature (see Figure S2), we used the very reliable permittivity determined from the lowest temperature to calculate all d_2 values.

In a first approach, we may assume bulk permittivity also for C_2 and then an effective thickness d_2 of the corresponding resistive regions can be determined. This type of analysis is very common for grain boundaries (brick layer model)[12,21] and leads to the thickness values shown in Figure 12. The nominal thickness d_2 strongly varies between samples and a systematic trend with annealing is not obvious. However, the constant phase elements CPE_2 of several samples exhibit very low exponents (average of $n < 0.6$); those samples are indicated in Figure 12. The most reliable C_2 values consistently and lead to a thickness d_2 of ca. 10-20 µm, independent of annealing.

The corresponding resistive region might be serially distributed within the entire sample (*e.g.*, several serial grain boundaries) or could be located at the two electrode/electrolyte interfaces. In order to further analyze the position, we removed ca. 1/5 of a sample by grinding both sample sides and measured the impedance again (resulting spectrum is shown in Figure S4). Obviously, some changes compared to the originally annealed sample exist, but the

intermediate frequency arc is still present and of similar size as before. This suggests that the resistive region is not restricted to a zone near the electrodes, but rather is an effect that includes regions within the entire sample, most probably, the grain boundaries.

The measurement of a $Zr_{1.75}Mo_{0.25}$ sample with Li electrodes strongly supports this interpretation. Figure 13 displays the corresponding impedance spectrum. While the high and intermediate frequency arcs are again clearly visible, the low frequency electrode response shrank to a tiny feature at very low frequencies.

The latter is typical for Li electrodes[18,22] but not further considered here. Two serial R-CPE elements fit the data well (solid line) and interpretation of R_1 in terms of the bulk conductivity leads to $\sigma_{bulk} = 2.4 \times 10^{-4}$ S cm^{-1}. This is in good agreement with measurements using Pt/Ti electrodes, particularly in consideration of the fact that a sample of a different batch was analyzed and a variation of the conductivity between different batches was also found for Pt/Ti electrodes, see Figures S3.

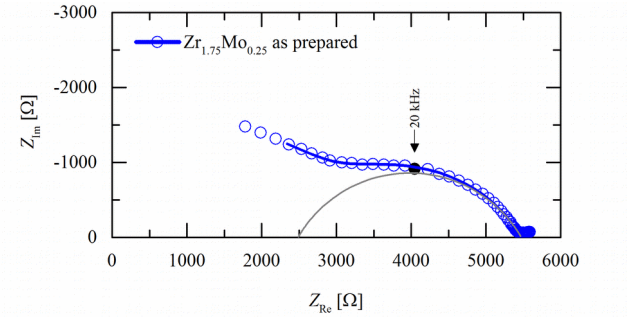

Figure 13. Nyquist plots of symmetrical cells containing pellets sandwiched between lithium electrodes and fit line using two serial R-CPE elements

The capacitance of the intermediate frequency arc can be determined from Eq. (2) and the resulting value corresponds to a thickness of ca. 7 µm (assuming $\varepsilon_r = 50$, see Figure S2), which is in excellent agreement with the measurements using Pt/Ti electrodes. The area-specific capacitance is about two orders of magnitude smaller than that of Li/LLZO interfacial arcs found for similarly prepared electrodes on Al-doped LLZO.[18] The area-specific resistance of the arc in Figure 13 is much larger than that of a Li/LLZO interface prepared in Ar[18] but fits well to that found for Ti/Pt electrodes. This supports our conclusion that the large intermediate frequency arc of our study is not primarily caused by the Li/LLZO interface but largely originates from regions within the LLZO sample, probably grain boundaries. (A smaller Li/LLZO interfacial arc might still exist but cannot be separated from the large intermediate frequency arc). If R_2 is the grain boundary resistance (R_{gb}), we can calculate the corresponding grain boundary thickness δ_{gb} from the total thickness d_2 and the grain size L_g according to

$$\delta_{gb} = d_2 / L_g d \quad . \tag{5}$$

When using the estimates of grain sizes given above, Eq. (5) leads to δ_{gb} values of the order of 1 µm and thus to a thickness that is much larger than typically found for the structurally disordered grain boundary core region of oxides (a few nm). It is also significantly larger than a space charge width expected for a highly Li-ion conductive material with high concentration of mobile charge carriers. Still other effects close to grain boundaries could lead to such a thickness, *e.g.*, a Li^+-H^+ exchange mechanism.[23]

For the sake of clarity it is worth mentioning that the correctness of the calculated thickness d_2 and thus of δ_{gb} depends on the correct assumption of the permittivity. If, for example, many voids and gaps exist between grains, the current may become constricted to a few contact points and a very inhomogeneous and frequency dependent current distribution results. This has been treated in detail in finite element studies and may also cause intermediate frequency arcs with capacitances being determined by the voids and thus by $\varepsilon_r = 1$.[24] In our case d_2 values would then decrease by a factor of 50. However, microstructural images and the strong increase of R_2 with annealing do not support such an interpretation in terms of voids/pores.

3.6.5 The Li-ion conductivity of resistive zones in Mo-doped LLZO

Assuming the appropriateness of the assumptions $\varepsilon_2 \approx \varepsilon_1$ and homogeneous current flow, a Li-ion conductivity of the resistive region (presumably at grain boundaries) can finally be calculated, irrespective of the transport mechanism and location. Arrhenius diagrams of these conductivities are shown for all samples in Figure 14. Activation energies are similar to those of the bulk conductivity, typically in the 0.4-0.5 eV range, partly up to 0.66 eV (see Table 1). Li-ion conductivities at RT are of the order of 10^{-5} to 10^{-7} S cm^{-1}, depending on composition and annealing, and thus many orders of magnitude lower than the Li-ion bulk conductivity. A similar value is found for the Li/Garnet/Li sample (ca. 5×10^{-7} S cm^{-1}). (Note that this is the true conductivity of the resistive zone. When considering effective sample conductivities, the resistance R_2 has to be normalized to the entire sample thickness.) The very low conductivity of the resistive zone indicates that it is highly important for any application to understand and ultimately reduce or eliminate this effect.

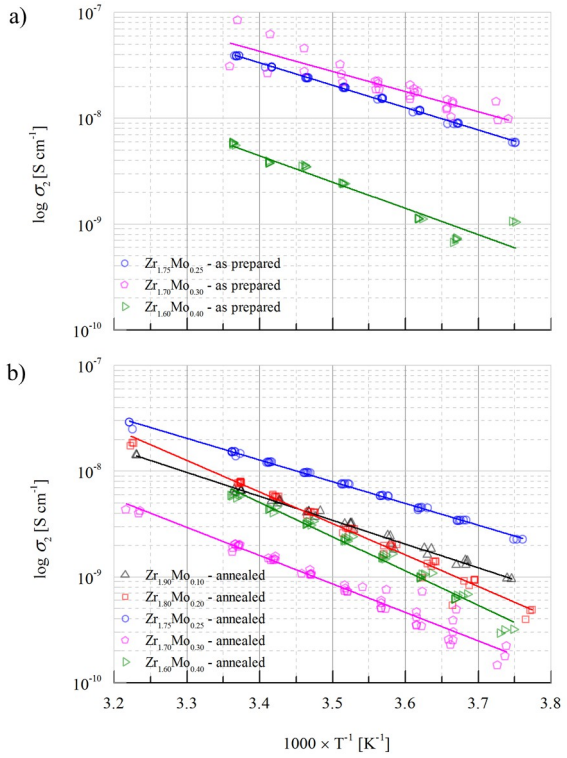

Figure 14. Temperature dependent Li-ion conductivity of the process causing the intermediate frequency arc of differently doped LLZO samples, as prepared (a) and after annealing at 700°C (b). The values are calculated from the thicknesses in Figure S5 and measured R_2 values.

3.7 Electrochemical stability measured by CV

Finally we checked the electrochemical stability of Mo-doped LLZO. Therefore a cyclic voltammetry experiment on a Li/$Zr_{1.75}Mo_{0.25}$/Au cell was measured to investigate the electrochemical window of the garnet pellet.

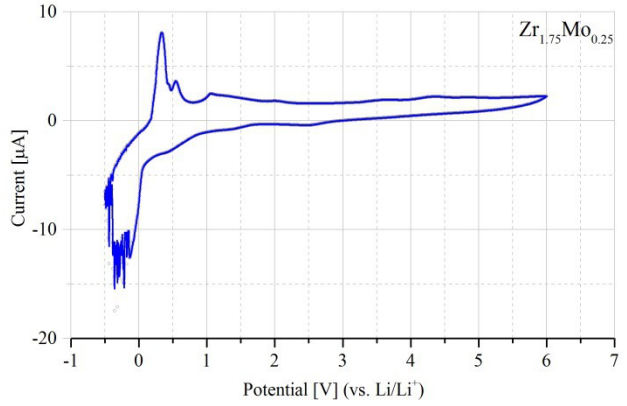

Figure 15. Cyclic voltammogram of Li/$Zr_{1.75}Mo_{0.25}$/Au cell at scan rate of 2mV/min in the potential range from -0.5V to 6V vs. Li/Li$^+$.

As shown in Figure 15 peaks due to an alloying reaction between Au and Li and extraction of Li from the alloy were clearly observed without obvious peaks at higher voltages, indicating that Li$^+$ could pass through the garnet pellet without possible degradation reactions. During the anodic sweep of the CV experiment, the garnet was found to be stable up to 6V.

4. Conclusion

Cubic $Li_{7-2x}La_3Zr_{2-x}Mo_xO_{12}$ garnets were synthesized using ceramic sintering methods. Since Mo^{6+} substitutes for twice as much Li^+ as Ta^{5+} does, about 0.25 Mo^{6+} is enough to decrease the Li^+ content to the critical amount of ≤ 6.5 Li^+ pfu, which stabilizes the cubic LLZO garnet phase. The solubility limit of Mo^{6+} in LLZO is about 0.3 pfu, lower than that of other supervalent ions that substitute for Zr^{4+}. Mo^{6+} has a smaller ionic radius than Zr^{4+} and is located at the 16*a* site of the cubic oxygen garnet framework causing the unit-cell parameter, a_0, to decrease as a function of the Mo^{6+} content. The highest σ_{bulk} is found for 0.25 Mo^{6+} pfu LLZO (ca. 3 × 10^{-4} S cm^{-1} at RT with significant variation for nominally identical samples). An intermediate frequency arc was found in the impedance spectra and its detailed analysis indicates that it differs from the interface-related additional arc found in some studies on LLZO. Rather, the additional resistance can be associated with resistive zones in the sample, most probably grain boundaries, and lowers the effective Li-ion conductivities. It is thus highly important for any application to not only control the interfacial resistance at the electrodes but also to understand and ultimately reduce or eliminate any additional resistance within the sample. Finally the voltage stability window of Mo^{6+} doped LLZO was checked and found to be about 6 V, which enables the use of high voltage cathode materials.

ASSOCIATED CONTENT

Supporting Information. This material is available free of charge via the Internet at http://pubs.acs.org.

Results from impedance spectroscopy of (i) samples after annealing, (ii) different prepared samples, and (iii) a sample measured at various times. Results from bulk permittivities as a function of temperature.

AUTHOR INFORMATION

Corresponding Author

* daniel.rettenwander@sbg.ac.at

Author Contributions

The manuscript was written through contributions of all authors. / All authors have given approval to the final version of the manuscript.

Funding Sources

The research was supported by Austrian Science Fund (FWF): project number P25702.

ACKNOWLEDGMENT

We are grateful to ILL for making all facilities available. The portion of the work performed at LBNL was supported by the Assistant Secretary for Energy Efficiency and Renewable Energy, Office of Vehicle Technologies of the U.S. Department of Energy under contract no. DE-AC02-05CH11231.

REFERENCES

(1) Awaka, J.; Kijima, N.; Hayakawa, H.; Akimoto, J. *Synthesis and structure analysis of tetragonal $Li_7La_3Zr_2O_{12}$ with the garnet-related type structure: J. Solid State Chem.* **2009**, *182*, 2046-2052.

(2) Awaka, J.; Takashima, A.; Hayakawa, H.; Kijima, N.; Idemoto, Y.; Akimoto, J. *Single Crystal Synthesis of Cubic Garnet Related-Type $Li_7La_3Zr_2O_{12}$ by a Self-Flux Method: Key Eng. Mater.* **2011**, *485*, 99-102.

(3) Murugan, R.; Thangadurai, V. Weppner, W. *Fast Lithium Ion Conduction in Garnet-type $Li_7La_3Zr_2O_{12}$: Angew. Chem. Int. Ed.* **2007**, 46, 7778.

(4) Allen, J. L.; Wolfenstine, J.; Rangasamy, E.; Sakamoto, J. *Effect of substitution (Ta, Al, Ga) on the conductivity of $Li_7La_3Zr_2O_{12}$: J. Power Sources* **2012**, *206*, 315-319.

(5) Rettenwander, D.; Langer, J.; Schmidt, W.; Arrer, C.; Harris, K.; Terskikh, V.; Goward, G.; Wilkening, M.; Amthauer, G. *Chem. Mater.* **2015**, *27*, 3135–3142.

(6) Bottke, P.; Rettenwander, D.; Wilkening, M. *Li NMR spin-lattice relaxation and ion dynamics in oxide garnets serving as solid electrolytes: Chem. Mater.* **2015**, under review.

(7) Rodriguez-Carvajal, J. *Recent advances in magnetic structure determination by neutron powder diffraction: Physica B*, **1993**, 192, 55-69.

(8) Shannon, R. D.; Prewitt, C. T. *Effective Ionic Radii in Oxides and Fluorides: Acta Cryst.*, 1969, **B25**, 925-946.

(9) Zeier, W. G. *Structural limitations for optimizing garnet-type solid electrolytes: a perspective: Dalton Trans.* **2014**, 43, 16133-16138.

(10) Tietz, F.; Wegener, T.; Gerhards, M. T.; Giarola, M.; Mariotto, G. *Synthesis and Raman micro-spectroscopy investigation of $Li_7La_3Zr_2O_{12}$: Solid State Ionics* **2013**, *230*, 77-82.

(11) T. Thompson, J. Wolfenstine, J. L. Allen, M. Johannes, A. Huq, I. N. David, J. Sakamoto, Tetragonal vs. cubic phase stability in Al - free Ta doped $Li_7La_3Zr_2O_{12}$: *J. Mater. Chem. A*, **2014**, 2, 13431-13436.

(12) Fleig, J. *The grain boundary impedance of random microstructures: numerical simulations and implications for analysis of experimental data: Solid State Ionics*, 2002, 150, 181-193.

(13) Zhao, X.; Vanderbit, D. Phonons and lattice dielectric properties of zirconia: *Phys. Rev. B*, **2002**, 65, 075105-1-10.

(14) Fleig, J.; Maier, *J. Microcontact impedance measurements of individual highly conductive grain boundaries: General aspects and application to AgCl: Phys. Chem. Chem. Phys.*, **1999**, 1, 3315-3320.

(15) Maier, J. Ionic conduction in space charge regions: *Prog. Solid State Chem.*, **1995**, 23, 171-263.

(16) Thangadurai, V.; Narayanan, S.; Pinzaru, D. *Garnet-type solid-state fast Li-ion conductors for Li batteries: critical review: Chem. Soc. Rev*. **2014**, 43, 4714-4727.

(17) Tenhaeff, W.; Wyatt, E.; Rangasamy, E.; Wang, Y.; Sokolov, A. P.; Wolfenstine, J.; Sakamoto, J.; Dudney, N. J. *Resolving the Grain Boundary and Lattice Impedance of Hot-Pressed $Li_7La_3Zr_2O_{12}$ Garnet Electrolytes: Chem. Electro. Chem.*, **2014**, 1, 375-378.

(18) Cheng, L.; Crumlin, E. J.: Chen, W.; Qiao, R.; Hou, H.; Zorba, L.; Russo, V.; Kostecki, R.; Liu, R.; Persson, K.; Yang, W.; Cabana, J.; Richardson, T.; Chen, G.; Doeff, M. M. *The origin of high electrolyte-electrode interfacial resistances in lithium cells containing garnet type solid electrolytes: Phys. Chem. Chem. Phys.* **2014**, 16, 18294-18300.

(19) Buschmann, H.; Dölle, J.; Berendts, S.; Kuhn, A.; Bottke, P.; Wilkening, M.; Heitjans, P.; Senyshyn, A.; Ehrenberg, H.; Lotnyk, A.; Duppel, V.; Kienle, L.; Janek, J. *Structure and dynamics of the fast lithium ion conductor "$Li_7La_3Zr_2O_{12}$":Phys. Chem. Chem. Phys.* **2011**, *13*, 19378-19392.

(20) Cheng, L.; Chen, W.; Kunz, M.; Persson, K. A.; Tamura, N.; Chen, G.; Doeff, M. M. *Effect of Surface Microstructure on Electrochemical Performance of Garnet Solid Electrolytes: ACS Appl. Mater. & Interfaces* **2015**, 7, 2073-2081.

(21) Maier, J. *On the Conductivity of Polycrystalline Materials: Ber. Bunsenges. Phys. Chem.* **1986**, 90, 26-33.

(22) Buschmann, H.; Berendts, S.; Mogwitz, B.; Janek, J. *Lithium metal electrode kinetics and ionic conductivity of the solid lithium ion conductors "$Li_7La_3Zr_2O_{12}$" and $Li_{7-x}La_3Zr_{2-x}Ta_xO_{12}$ with garnet-type structure: J. Power Sources*, **2012**, 206, 236-244.

(23) Wang, Y.; Lai, W. *Phase transition in lithium garnet oxide ionic conductors $Li_7La_3Zr_2O_{12}$: The role of Ta substitution and H_2O/CO_2 exposure: J. Power S.*, **2015**, 275, S171-S176.

(24) Fleig, J.; Maier, J. *Finite-Element Calculations on the Impedance of Electroceramics with Highly Resistive Grain Boundaries: I, Laterally Inhomogeneous Grain Boundaries: J. Am. Ceram. Soc*. **1999**, 82, 3485-3493.

For Table of contents only

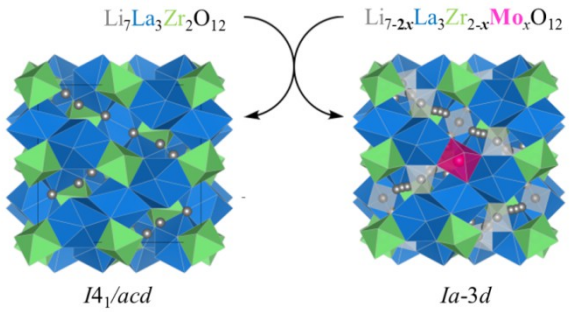

Synapsis

Cubic $Li_7La_3Zr_2O_{12}$ (LLZO) garnets are exceptionally well suited to be used as solid electrolytes or protecting layers in “Beyond Li-ion Battery” concepts. In this study we demonstrate a new possibility to stabilize the cubic phase at RT via substitution of Zr^{4+} by Mo^{6+}. Special attention was paid to the crystal chemical as well as electrochemical properties of the new material.